Nano-Chemical and Mechanical Mapping of Fine and Ultrafine Indoor Aerosols with Peak Force Infrared Microscopy

Joseph M. González-Fialkowski,[1] Le Wang,[1] Yongjie Li,[2] and Xiaoji G. Xu[1]*

1. Department of Chemistry, Lehigh University, 6 E Packer Ave. Bethlehem, PA, 18015
2. Department of Civil and Environmental Engineering, Faculty of Science and Technology, University of Macau, Avenida da Universidade, Taipa, Macau, China

*Email address: xgx214@lehigh.edu

Abstract

Indoor aerosols can adversely affect human health, as we increasingly spend more time indoors. One of the aerosol research challenges is detecting and measuring fine and ultrafine aerosol particles with nanoscale dimensions. Spectroscopic tools, often diffraction-limited, cannot access the intra-particle heterogeneity. In this work, we extend the non-invasive nanoscopy method of peak force infrared (PFIR) microscopy to study indoor aerosols. Lab-generated fine bioaerosols were collected after a surgical face mask to serve as a benchmark sample, followed by a variety of field-collected indoor aerosols with and without the filtration of a facemask. A general heterogeneity is observed in individual aerosol particles, despite their nanoscale dimension. The presence of protein, triglycerides, and salt are detected through chemical and mechanical mapping. The PFIR microscopy is suitable to identify the composition of fine and ultrafine aerosols. Its application is particularly meaningful for understanding the particle structure to reduce aerosol-related transmission of diseases.

Introduction

Aerosols, also known as particulate matter, are airborne entities having micro- to nanometer dimensions with heterogeneous intraparticle physical and chemical features. Although aerosols can have many origins and different compositions, an increasing focus of research is on the bioaerosols, i.e., aerosol particles with a biological or biochemical component in their compositions. Examples of bioaerosols range from large particles, such as pollens, to small entities, such as viruses. For instance, disease-causing viruses can be found in droplets generated through coughing and even regular conversations between people, situations related to the transmission of COVID-19.[1-3]

Indoor settings are prone to closed-quarter aerosol circulation due to the lack of ventilation.[4] While large indoor aerosol particles can be removed with regular air filters, small-size aerosols, termed fine and ultrafine particles, can penetrate air filters and are difficult to remove. Fine aerosols are classified as particulate matter with diameters of less than 2.5 microns ($PM_{2.5}$); ultrafine aerosols are classified as particulate matter with diameters of less than 0.1 microns ($PM_{0.1}$). Fine and ultrafine aerosols have the potential to negatively impact human health in several ways. Ultrafine particles are small enough to reach deep lung tissue and even translocate throughout organs when inhaled, leading to possible physical harm.[5] A recent study on the size fractionation of bioaerosol emissions from green-waste composting in indoor industrial facilities reported exposure to an abundance of actinobacteria having diameters of a couple of microns or less in air, suggesting the potential for allergenic respiratory issues and an overall need to better understand the presence of bioaerosols in a workplace environment.[6] Also, research has found that fine aerosol particles and ultrafine particles can suspend in the air for an extended period of time from minutes, hours, to even days, due to their low settling velocity. According to Stokes' Law, the smaller diameter the aerosols are, the longer the settling time is for the aerosols to reach the ground by gravity. Fine and ultrafine particles are less likely to settle than large-size aerosol particles in the air.

Although the compositions of aerosols correlate with the environment that they reside in, fine and ultrafine aerosols, because of their long settling time and airborne mobility, can diffuse over long distances and accumulate over time. As a result, the types and chemical compositions of fine and ultrafine aerosol particles are not necessarily determined by their residing environment. In indoor settings, the sources of bioaerosols are not local. The presence of aerosols is caused by human activities and is affected by ventilation.[7] The characterization of aerosols requires access to individual aerosol particles to determine their compositions and organization. Also,

aerosols can have heterogeneous regions of chemical compositions, varying mechanical properties, and even regions of different physical states, such as solid/liquid phase separations.[8, 9] Revealing intra-particle heterogeneity requires analytical methods of high spatial resolution.

A wide range of analytical chemistry methods has been utilized to study aerosols. They have their respective strength and associated limitations. The size and shape distribution of large quantities of aerosol particles is measured by the light scattering method without the need for aerosol collections.[10] Optical microscopy allows for the quick visual examination of large size aerosol particles. The spectroscopy methods of infrared (IR) microscopy and Raman spectroscopy allow for non-destructive chemical identification of aerosol particles, although bound by the diffraction limit.[11-13] Electron microscopy (EM) and atomic force microscopy (AFM) provide excellent spatial resolution below the optical diffraction limit, particularly suitable for fine and ultrafine aerosol particles.[14-16] Time-of-flight secondary ion mass spectrometry (ToF-SIMS) enables chemical analysis of individual aerosol particles at several tens of nanometers spatial resolution, although mass spectrometry often requires destroying the particle during analysis.[17, 18]

The AFM-based infrared (AFM-IR) microscopy provides a non-destructive, high spatial resolution chemical imaging route to characterize aerosol particles. AFM-IR refers to a collection of AFM-based infrared microscopy methods that use a sharp AFM tip to mechanically probe the photothermal response of the sample in the infrared frequency range.[19] In AFM-IR, infrared pulses illuminate the sample underneath a metallic AFM tip. The relaxation of infrared absorption in the sample usually leads to photothermal expansion, which pushes the AFM tip, causing the AFM cantilever to bend and oscillate. By detecting the cantilever mechanical response, the signal proportional to the thermal expansion caused by infrared absorption is detected. The signal magnitude is dependent on the infrared absorption coefficient and the photothermal expansion coefficient. Given that the thermal expansion coefficients do not depend on the infrared excitation wavelength, the AFM-IR signal versus the wavelength gives a good correspondence to the infrared absorption spectrum. Because no optical detection is involved in AFM-IR, the sharp AFM tip delivers a route to overcome the optical diffraction limit to reach a high spatial resolution to tens of nanometer scale. Since its invention,[20, 21] three major routes of AFM-IR techniques have been developed based on the AFM modes: the contact mode, the tapping mode, and the peak force tapping mode. The contact mode AFM-IR has been used by Dr. Andrew Ault and coworkers to distinguish organic and inorganic regions within a single aerosol particle at a spatial resolution of less than 100 nm.[8] They also have successfully characterized phase-separated core-shell

particles by their molecular information obtained using AFM-IR. Our research group has applied peak force infrared (PFIR) microscopy, right after its invention,[22] to identify the secondary organic aerosols collected at an urban center.[23] Compared with contact mode AFM-IR, the PFIR microscopy has a better spatial resolution, less surface damage to the sample, and provides complementary mechanical properties. The spatial resolution of the PFIR microscopy has been demonstrated to be ~ 6 nm spatial resolution on representative samples.[24, 25] However, PFIR has not yet been applied to characterize indoor aerosols or ultrafine particles in particular. As the technical capability of PFIR continues to be improved over the years,[26-28] PFIR is ready to be applied in these areas to contribute to aerosol studies.

In this work, we utilized PFIR microscopy to measure the chemical compositions and mechanical properties of indoor-collected aerosols. Laboratory generated aerosols from reference protein samples were collected behind a surgical face mask and imaged with the PFIR microscopy. Then, individual field-collected indoor aerosols from a grocery store were imaged with the PFIR microscopy. Intraparticle chemical and mechanical heterogeneity was observed. Besides the proof of principle on nanoscale infrared imaging, our measurement also demonstrates that some fine and ultrafine particles can pass through a surgical mask. Better masks are required to reduce the exposure of indoor fine and ultrafine bioaerosols.

Methods

Lab generation and collection of aerosols

An aerosol generation and collection apparatus were assembled in a ventilated fume food. Figure 1 displays the schematics of the apparatus. Bovine Serum Albumin (BSA) was chosen as the reference composition for bioaerosol generation because of its accessibility and characteristic infrared signatures of amide bonds. A 1% BSA solution was prepared in distilled water under ambient conditions from lyophilized BSA-fraction V (Rockland Antibodies & Assays). The solution was stored in a refrigerator (4 ºC) prior to use for aerosol production. The BSA for use was removed from storage and allowed to reach room temperature prior to aerosol generation.

BSA aerosols were generated using a bubble-tank generator (Atomizer Aerosol Generator ATM 228, Topas). The pressure was set at an outward flow of 1200-1400 mbar, mimicking that of human breathing pressures.[29] The relative humidity of the ambient was between 40% to 60%. A detailed procedure of aerosol generation protocol is described in the literature.[30] At a fixed

distance of about 0.5 m away from the generator was a three-stage particle sampler (Particle Sampler MPS-3, California Measurements). The distance of 0.5 m is chosen because it represents the distance between two adjacent students in a classroom before social distancing. Each stage of the particle sampler successively filters particulate matter (PM) by order of diameter in microns. The first, second, and third stages correspond to PM_{10}, $PM_{2.5}$, and $PM_{0.1}$, respectively. A surgical-grade facemask was placed directly in front of the sampler inlet for all collections. Silicon substrates were used to collect BSA aerosols for impaction. Substrates were fixed in either stage two or three and exposed to aerosol for 30 to 60 seconds. Samples were stored in an air-tight container before the PFIR analysis.

Field aerosol collection

Field aerosol samples were acquired at a local grocery store in Bethlehem, PA as well as in residential houses and office space. For the aerosol collection at the grocery store, a surgical-grade facemask was placed directly in front of the inlet of the three-stage aerosol sampler (MPS-3). The relative humidity were within the range of 40% to 60%, regulated by the heating, ventilation, and air conditioning systems of the buildings. The collection locations, stages, and durations of the particle sampler are listed in Table S1 of the Supporting Information. Silicon substrate was fixed in either stage two or three for collection. After collection, substrates with samples were transferred to an air-tight container for the PFIR measurement later. Collection details are located in the Supplemental Information (SI).

PFIR apparatus

The apparatus of the PFIR microscope consists of a frequency tunable infrared laser, a peak force tapping (PFT) enabled AFM, and custom-built time synchronization and signal processing device. As a new type of AFM-IR, the PFIR microscopy delivers simultaneous infrared and mechanical mapping at ~ 6 nm spatial resolution. The details on how to construct and operate the PFIR microscopy are described in the literature. Figure 2a schematically displays the operational principle of the PFIR microscopy. A stage-scan AFM (Multimode 8, Bruker) is operated in the PFT mode with a peak force set point at 5 nN. A platinum-coated AFM tip (HQ.:NSC14/Pt, Mikromasch) with a 160 kHz resonant frequency and 5 N/m spring constant is used. The vertical position of the sample stage that holds aerosol particles oscillates up and down at the PFT frequency of 2 kHz. The same PFT frequency is routed to a phase lock loop (HF2Li Zurich Instrument) and used to trigger laser emissions from a quantum cascade laser (QCL, MIRcat-QT D.R.S. Daylight Solutions). The timing of the laser emission is synchronized when the

tip and sample are in dynamic contact. The infrared frequency of the QCL is tunable between 1370 cm^{-1} to 1780 cm^{-1}, and the pulse duration used was 500 ns at a current of 1050 mA at a repetition rate of 2 kHz. The infrared absorption of the sample and subsequent vibrational energy relaxation leads to the photothermal expansion of the sample due to rapid temperature increase, causing the cantilever of the AFM probe to oscillate at its resonant frequencies. A quadrant photodiode reads out the dynamic cantilever deflection signals in the time domain and is digitalized by a data acquisition card (PXI-5122, National Instruments). Figure 2b displays a representative cantilever dynamic deflection signal. The signal is processed with a software program written in Labview in an embedded computer (PXIe-8135, National Instruments) connected to the data acquisition card. The slow cantilever deflection due to the tip indentation to the sample in the PFT cycle is fitted with a polynomial and removed to obtain the cantilever oscillations due to laser-induced photothermal response of the sample (Figure 2c). A fast Fourier Transform (FFT) is used to convert the cantilever oscillations into the frequency domain (Figure 2d). The response across the cantilever resonance in the frequency domain is integrated to obtain the PFIR signal. The imaging is done by registering the PFIR signal during the AFM lateral scan; the spectra are collected by recording the PFIR signal while sweeping the frequency of the QCL within its tuning range.

While traditional AFM tapping mode yield the tapping phase together with the topography information, the tapping phase lacks quantitative correspondence to the mechanical property of the sample. The PFIR microscopy operates in the peak force tapping mode. Complimentary mechanical properties from the PeakForce Quantitative Nanomechanical Mapping (PeakForce QNM)[31] are simultaneously registered with the PFIR measurement. The mechanical modulus is obtained from Derjaguin-Muller-Toporov (DMT) model,[32] and the adhesion is obtained as averaged detachment force between the AFM tip and the sample during PFT cycles.

Results

PFIR measurement of lab-generated aerosol particles from BSA.

Figure 3a displays the topography of a lab-generated bioaerosol particle from the BSA solution. The aerosol particle was collected from the third stage of the aerosol sampler that corresponds to $PM_{0.1}$. The topography of this aerosol particle has a lateral dimension of 90 nm by 170 nm, and a height of 25 nm. A map of logarithmic of the modulus is shown in Figure 3b, collected from the complementary PeakForce Quantitative Nanomechanical mapping with the

peak force tapping mode. Figure 3c displays the PFIR image of the BSA aerosol at 1660 cm^{-1} infrared frequency that is resonant with the amide bond of the protein. Figure 3d shows the off-resonant PFIR image collected at 1450 cm^{-1}, which shows a lack of infrared absorption when off-resonance. Figure 3e displays a PFIR spectrum collected from the location marked by the star in Figure 3a. Characteristic peaks of infrared absorption of amide bonds are observed. The right side of the fine aerosol shows an increased amide infrared signal, confirming the presence of the BSA. In terms of spatial distributions, the modulus map in Figure 3b shows that the left side of the aerosol particle appears to be more rigid than the right side of the particle; the on resonant PFIR image at 1660 cm^{-1} also shows that the left side of the particle lacks the amide infrared response. The correlative maps of both the infrared channel and the mechanical channels indicating that the left side of the particle is not BSA. It could be a nanoscale cluster of inorganic salt that is commonly found to serve as a site for aerosols to grow, even for these indoor lab-generated aerosols. The left side of the particle could also be from organic matters of high modulus that also lack amide response. The right side of the aerosol particle has a high infrared response at amide bond and low modulus, which is consistent with the properties of BSA protein. Figure 3f displays sectional plots of modulus and amide infrared response along the dashed line in Figure 3a, across the possibly salt region and the protein region of this aerosol particle.

Note that in our PFIR measurement of Figure 3, there are several smaller clusters of proteins around the large central aerosol. The dimensions of these protein clusters are several tens of nanometers. Some of them are even as small as 20 nm in diameter (e.g., the ultrafine aerosol marked by the white arrow in Figure 3c). The detection of these ultrafine bioaerosols demonstrates the spatial resolution of the PFIR microscopy.

Measurement and analysis of field-collected indoor aerosols

After benchmarking the capabilities of PFIR on measuring lab-generated aerosol particles, field-collected aerosol particles were studied. The measurement of a field-collected sample from a local grocery store is shown in Figure 4. The aerosol particle was collected from the third stage of the aerosol particle sampler, corresponding to aerodynamic diameters of less than 100 nm. Figure 4a displays the AFM topography of the field-collected indoor aerosol particle. The lateral dimensions of the aerosol particle from the topography are about 250 nm with a height of about 60 nm. The surface of the aerosol particles exhibits grainy features, suggesting that the particle is a conglomeration of several small particles, possibly with different chemical identities. The

variations of surface adhesion (Figure 4b) also indicate the possible variation of chemical compositions. The PFIR image at 1660 cm^{-1}, which corresponds to the amide bond of protein, is displayed in Figure 4b. It shows a heterogeneous response of the infrared absorption. The PFIR image at 1450 cm^{-1}, which corresponds to a C-H scissoring infrared response of organic molecules, is shown in Figure 4c. They are observed between the grains of the smaller constituent particles that form the large aerosol particle. The C-H rich organic molecules are likely binding the small particles together in the growth of the field-collected aerosol and serve as a coating to encapsulate aerosol particles. A likely candidate of the organic molecule is fatty acids, which are found in cooking oil that is likely to be present in the indoor environment. The adhesion image in Figure 4b exhibits strong spatial correlations with the amide infrared response in Figure 4c, suggesting adhesion force between the protein and the AFM tip is stronger than the adhesion force between the Si substrate and the tip. The spatial heterogeneity of the aerosol particle is further revealed by spectra from three different locations of this aerosol particle. Figure 4e displays three spectra that are collected at the surface of the aerosol particle. Location 1 exhibits a spectral signature close to 1400 cm^{-1}, possibly due to the presence of the ammonium sulfate, which is one of the most abundant inorganic salts in aerosols. Locations 2 and 3 show characteristic infrared responses of the amide bond, which means this field-collected particle belongs to the categories of bioaerosol, but agglomerates with at least one inorganic (ammonium sulfate) particle.

A larger aerosol particle from the second stage of the particle collector was also studied with PFIR microscopy. The second stage corresponds to particles with an aerodynamic diameter between 100 nm and 2.5 μm. Figure 5 displays the PFIR measurement of the aerosol particle. A Figure 5a shows the AFM topography of this particle of the lateral dimension of 400 nm and a height of about 50 nm, which is formed from a cluster of smaller grains. The adhesion map is displayed in Figure 5b, which shows heterogeneity: a region of several grains on the right if the aerosol particle exhibits a reduced adhesion, suggesting different composition. The complementary modulus image is displayed in Figure 5c. Spatial variations of the moduli are observed. The PFIR image at an infrared frequency of 1660 cm^{-1} is displayed in Figure 5d. Grains that contain proteins are spatially revealed. Two PFIR spectra were collected on the aerosol particle at locations marked by 1 and 2 in Figure 5a. The PFIR spectra are displayed in Figure 5e. A clear contrast of the infrared responses is observed at these two spatial locations. The spectrum at Location 2 contains infrared responses at 1730 cm^{-1}, which corresponds to the carbonyl functional group. It corresponds to the high adhesion, high modulus region of this aerosol particle. A possible source of this chemical component may be from the oxidization, unsaturated

fatty acid reacting with ozone to form products that contain carbonyl group. The PFIR spectrum at location 1 carries the signatures of protein, suggesting partial biological origins. The heterogeneous and grainy composition of this fine aerosol particle confirms that indoor aerosol particles growth can be formed through the clustering of even smaller ultrafine particles. The white arrows in Figure 5c and 5d show one possible ultrafine particle of ~50 nm in diameter. It has similar amide infrared response and mechanical properties as the right side of the large fine aerosol particle, indicating a similar origin. A three-dimensional representation the PFIR signal overlaid on topography of the same data of Figure 5 is included in Supplementary Figure S1, for an alternative illustration of the chemical distribution of aerosol particles.

Field-collected indoor aerosols without filtration by face mask

Because surgical face masks can effectively filter out large aerosol particles, large size indoor aerosol particles were collected without the filtration of a face mask. Figure 6 shows the PFIR measurement of irregular shape aerosols collected in a residential house with the second stage of the aerosol collector. The parameters of the collection are described in Supplementary Table S1. Figure 6a displays the AFM topography of the non-spherical aerosol particle about 750 nm in length, with an average width of around 160 nm and a height of 85 nm. The co-registered adhesion map is displayed in Figure 6b, which reveals a level of surface heterogeneity. The PFIR image at an infrared frequency of 1725 cm^{-1} is displayed in Figure 6c, and the PFIR image at 1660 cm^{-1} is displayed in Figure 6d. In contrast to field-collected aerosol particles in Figure 4 and Figure 5 that contains rich in proteins, this field-collected aerosol in Figure 6 has a dominant carbonyl infrared response at 1725 cm^{-1} and absence of protein infrared response at 1660 cm^{-1}. The spectra collected at two locations on this aerosol particle are shown in Figure 6e. The shape and chemical composition of this aerosol particle cluster suggest it could be a soot agglomerate that contains oxidized carbonyl species.[33] The residential house, in which the aerosols were collected, has a wood stove for supplementary heating. It may generate fine soot aerosols that are levitated in air over extend period.

Figure 7 displays another field-collected aerosol particle of non-spherical shapes. Figure 7a shows the topography of an aerosol particle that resembles a fragment of a flake with a relatively flat surface. The particle also exhibits a relatively homogeneous surface adhesion (Figure 7b). The PFIR images at 1660 cm^{-1} and 1725 cm^{-1} infrared frequencies are displayed in Figure 7c and Figure 7d, respectively. The infrared imaging reveals that the majority of the particles is made of protein. Carbonyl responses that may associate with triglyceride are only present at the lower left side of this particle. Figure 7e is the plots of two PFIR spectra obtained

from the two locations in Figure 7a. The spectra bear a high resemblance. The homogeneity of this aerosol particle from both the adhesion channel and the infrared channels suggests that this particle is likely generated from the breakdown of a larger structure of biological origin rather than growth from convalescent of smaller particles, such as in Figures 4-6. The likely candidate of origin for this biological aerosol particle may be a small fragment of skin that are commonly present indoor.

Discussion

Fine aerosol particles in Figure 3 to Figure 5 were collected after the filtration of a surgical face mask. Their presence on the collection stages confirms that even with the filtration from a surgical face mask, some fine biological aerosol particles of ~100 nm or less can still pass through. Given the fact that airborne viruses have a dimension of ~100 nm, our measurement indicates the potential of penetration of fine aerosols (such as aerosols with a size of a SARS-CoV-2 virus) even with the protection of a surgical face mask. Masks of a better grade, e.g., N95 or KN95, offer better protection to block these fine aerosol particles and should be encouraged to use.[34]

From the perspective of the characterization method, PFIR microscopy is advantageous for non-destructive multimodal chemical and mechanical imaging of fine and ultrafine aerosol particles. It delivers high spatial resolution for the measurement of fine and ultrafine aerosol particles bypassing the optical diffraction limit that restricts conventional infrared and Raman microscopy. The ~10 nm spatial resolution of the PFIR microscopy matches well for fine and ultrafine aerosol particles down to 100 nm in dimensions, which are the scales of a virus. The PFIR measurement does not consume or ionize the particle of interest during the measurement, unlike the mass spectrometry that requires ablation and ionization. The complementary mechanical information from the PFIR microscopy is obtained together with the infrared channel. The multimodal measurements provide additional correlations to deduce the constituent composition of aerosol particles. Compared with existing contact mode AFM-IR microscopy, the PFIR microscopy has an improved spatial resolution and avoids the lateral force between the tip and sample that often scratches the sample surface.

One consistent discrepancy is the size of AFM-measured particles and that from the aerosol particle sampler. Aerosol particles from Figure 3 and Figure 4 were collected from the third stage of the sampler, which corresponds to an aerodynamic diameter of less than 100 nm (ultrafine aerosol particles or $PM_{0.1}$). However, their AFM topography images have at least one dimension larger than 100 nm. This discrepancy can be understood by the measurement

mechanism of the AFM. When the aerosol particles are levitated in the air, they assume a spherical shape to minimize their surface areas to reduce surface energy. When the particles are collected by the planar substrate, they deform into a more disk-like shape, increasing their lateral dimensions and reducing their height. Also, the AFM measurement on the lateral dimension also contains convolution of the radius of the AFM probe, which in our case, is 25 to 30 nm (H.Q.:NSC14/Pt, Mikromasch). Therefore, the particle of Figure 3 is likely to belong to the ultrafine aerosol particle categories, and the particle in Figure 4 is at the borderline between ultrafine and fine aerosol particles when levitated in the air. Moreover, the particle sizes from each stage of the particle sampler have a distribution. Aerosol particles can go to either stage if their sizes are at the borderline.

Our experimental findings on individual indoor aerosol particles suggest the presence of a range of chemical compositions. The compositions of fine indoor aerosol include particles that contain the infrared signature of amide bonds, suggesting the presence of proteins; particles made of organic components with carbonyl infrared signature suggest primary emission (e.g., cooking) and secondary formation (e.g., ozonolysis); salt of ammonium sulfate that can mix with organic/biological particles. The presence of these compositions can be interpreted based on the indoor settings. The protein composition is likely due to biological origins, droplets from respiration, skin fragments etc. The carbonyl composition is possibly from triglyceride, which is commonly present due to cooking where oil is used. The ammonium sulfate particles are likely penetrated from the outdoor environment.

Fine aerosol particles collected after filtration by a surgical mask tend to have an overall spherical shape, as observed in Figure 4 and Figure 5; particles collected without mask filtrations are more likely to assume irregular, non-spherical shape, as shown in Figure 6 and Figure 7. It is possibly due to the filtration mechanism. Spherical shape aerosol particles are more permeable through the space between fabrics of a surgical mask; rod-like or flake-like particles are more likely to be blocked by the interwoven fabrics of a surgical mask. Therefore, we observe much fewer irregular-shaped aerosol particles after surgical mask filtrations.

In sum, PFIR microscopy delivers the high spatial resolution analytical method for investigating the composition distributions within fine and ultrafine aerosols. The joint chemical imaging and mechanical property mapping allow for the deduction of the possible origin of aerosol particles, including those collected from indoor.

Supporting Information

The Supporting Information is available free of charge on the ACS Publications website. The Supporting Information includes Supplementary Table S1 on collection parameters of the aerosol samples and Supplementary Figure S1 on 3D representation of the aerosol heterogeneity.

Acknowledgments

J.M.G-F, L. W. and X.G.X would like to thank the support from the National Science Foundation CHE 1847765. X.G.X. would like to thank the support of the Sloan Research Fellowship from the Alfred P. Sloan Foundation.

References:

1. Anderson, E. L.; Turnham, P.; Griffin, J. R.; Clarke, C. C., Consideration of the aerosol transmission for COVID-19 and public health. *Risk Analysis* **2020,** *40* (5), 902-907.
2. Tang, S.; Mao, Y.; Jones, R. M.; Tan, Q.; Ji, J. S.; Li, N.; Shen, J.; Lv, Y.; Pan, L.; Ding, P., Aerosol transmission of SARS-CoV-2? Evidence, prevention and control. *Environment International* **2020,** *144*, 106039.
3. Santarpia, J. L.; Rivera, D. N.; Herrera, V. L.; Morwitzer, M. J.; Creager, H. M.; Santarpia, G. W.; Crown, K. K.; Brett-Major, D. M.; Schnaubelt, E. R.; Broadhurst, M. J.; Lawler, J. V.; Reid, S. P.; Lowe, J. J., Aerosol and surface contamination of SARS-CoV-2 observed in quarantine and isolation care. *Scientific Reports* **2020,** *10* (1), 12732.
4. Prather, K. A.; Wang, C. C.; Schooley, R. T., Reducing transmission of SARS-CoV-2. *Science* **2020,** *368* (6498), 1422-1424.
5. Schraufnagel, D. E., The health effects of ultrafine particles. *Experimental & Molecular Medicine* **2020,** *52* (3), 311-317.
6. Ferguson, R. M. W.; Neath, C. E. E.; Nasir, Z. A.; Garcia-Alcega, S.; Tyrrel, S.; Coulon, F.; Dumbrell, A. J.; Colbeck, I.; Whitby, C., Size fractionation of bioaerosol emissions from green-waste composting. *Environment International* **2021,** *147*, 106327.
7. Morawska, L.; Tang, J. W.; Bahnfleth, W.; Bluyssen, P. M.; Boerstra, A.; Buonanno, G.; Cao, J.; Dancer, S.; Floto, A.; Franchimon, F., How can airborne transmission of COVID-19 indoors be minimised? *Environment International* **2020,** *142*, 105832.
8. Bondy, A. L.; Kirpes, R. M.; Merzel, R. L.; Pratt, K. A.; Banaszak Holl, M. M.; Ault, A. P., Atomic force microscopy-infrared spectroscopy of individual atmospheric aerosol particles: subdiffraction limit vibrational spectroscopy and morphological analysis. *Analytical chemistry* **2017,** *89* (17), 8594-8598.
9. Lee, H. D.; Wigley, S.; Lee, C.; Or, V. W.; Hasenecz, E. S.; Stone, E. A.; Grassian, V. H.; Prather, K. A.; Tivanski, A. V., Physicochemical Mixing State of Sea Spray Aerosols: Morphologies Exhibit Size Dependence. *ACS Earth and Space Chemistry* **2020,** *4* (9), 1604-1611.
10. Ault, A. P.; Axson, J. L., Atmospheric aerosol chemistry: Spectroscopic and microscopic advances. *Analytical Chemistry* **2017,** *89* (1), 430-452.
11. Sze, S. K.; Siddique, N.; Sloan, J. J.; Escribano, R., Raman spectroscopic characterization of carbonaceous aerosols. *Atmospheric Environment* **2001,** *35* (3), 561-568.
12. Lee, A. K. Y.; Chan, C. K., Single particle Raman spectroscopy for investigating atmospheric heterogeneous reactions of organic aerosols. *Atmospheric Environment* **2007,** *41* (22), 4611-4621.

13. Kaufman, Y. J.; Remer, L. A., Detection of forests using mid-IR reflectance: an application for aerosol studies. *IEEE Transactions on Geoscience and Remote Sensing* **1994,** *32* (3), 672-683.
14. Ebert, M.; Müller-Ebert, D.; Benker, N.; Weinbruch, S., Source apportionment of aerosol particles near a steel plant by electron microscopy. *Journal of Environmental Monitoring* **2012,** *14* (12), 3257-3266.
15. Patterson, J. P.; Collins, D. B.; Michaud, J. M.; Axson, J. L.; Sultana, C. M.; Moser, T.; Dommer, A. C.; Conner, J.; Grassian, V. H.; Stokes, M. D., Sea spray aerosol structure and composition using cryogenic transmission electron microscopy. *ACS Central Science* **2016,** *2* (1), 40-47.
16. Lee, H. D.; Tivanski, A. V., Atomic force microscopy: an emerging tool in measuring the phase state and surface tension of individual aerosol particles. *Annual Review of Physical Chemistry* **2021,** *72*, 235-252.
17. He, L. Y.; Huang, X. F.; Xue, L.; Hu, M.; Lin, Y.; Zheng, J.; Zhang, R.; Zhang, Y. H., Submicron aerosol analysis and organic source apportionment in an urban atmosphere in Pearl River Delta of China using high-resolution aerosol mass spectrometry. *Journal of Geophysical Research: Atmospheres* **2011,** *116* (D12).
18. Tervahattu, H.; Juhanoja, J.; Kupiainen, K., Identification of an organic coating on marine aerosol particles by TOF-SIMS. *Journal of Geophysical Research: Atmospheres* **2002,** *107* (D16), ACH-18.
19. Kurouski, D.; Dazzi, A.; Zenobi, R.; Centrone, A., Infrared and Raman chemical imaging and spectroscopy at the nanoscale. *Chemical Society Reviews* **2020,** *49* (11), 3315-3347.
20. Dazzi, A.; Prazeres, R.; Glotin, F.; Ortega, J. M., Local infrared microspectroscopy with subwavelength spatial resolution with an atomic force microscope tip used as a photothermal sensor. *Optics Letters* **2005,** *30* (18), 2388-2390.
21. Anderson, M. S., Infrared Spectroscopy with an Atomic Force Microscope. *Applied Spectroscopy* **2000,** *54* (3), 349-352.
22. Wang, L.; Wang, H.; Wagner, M.; Yan, Y.; Jakob Devon, S.; Xu Xiaoji, G., Nanoscale simultaneous chemical and mechanical imaging via peak force infrared microscopy. *Science Advances 3* (6), e1700255.
23. Wang, L.; Huang, D.; Chan, C. K.; Li, Y. J.; Xu, X. G., Nanoscale spectroscopic and mechanical characterization of individual aerosol particles using peak force infrared microscopy. *Chemical Communications* **2017,** *53* (53), 7397-7400.
24. Jakob, D. S.; Wang, L.; Wang, H.; Xu, X. G., Spectro-Mechanical Characterizations of Kerogen Heterogeneity and Mechanical Properties of Source Rocks at 6 nm Spatial Resolution. *Analytical Chemistry* **2019,** *91* (14), 8883-8890.
25. Li, W.; Wang, H.; Xu, X. G.; Yu, Y., Simultaneous Nanoscale Imaging of Chemical and Architectural Heterogeneity on Yeast Cell Wall Particles. *Langmuir* **2020,** *36* (22), 6169-6177.
26. Wang, H.; González-Fialkowski, J. M.; Li, W.; Xie, Q.; Yu, Y.; Xu, X. G., Liquid-Phase Peak Force Infrared Microscopy for Chemical Nanoimaging and Spectroscopy. *Analytical Chemistry* **2021,** *93* (7), 3567-3575.
27. Wang, H.; Wang, L.; Janzen, E.; Edgar, J. H.; Xu, X. G., Total Internal Reflection Peak Force Infrared Microscopy. *Analytical Chemistry* **2020,** *93* (2), 731-736.
28. Jakob, D. S.; Wang, H.; Xu, X. G., Pulsed Force Kelvin Probe Force Microscopy. *ACS Nano* **2020,** *14* (4), 4839-4848.
29. Lausted, C. G.; Johnson, A. T.; Scott, W. H.; Johnson, M. M.; Coyne, K. M.; Coursey, D. C., Maximum static inspiratory and expiratory pressures with different lung volumes. *Biomedical Engineering Online* **2006,** *5* (1), 1-6.
30. Alsved, M.; Bourouiba, L.; Duchaine, C.; Löndahl, J.; Marr, L. C.; Parker, S. T.; Prussin, A. J.; Thomas, R. J., Natural sources and experimental generation of bioaerosols: challenges and perspectives. *Aerosol Science and Technology* **2020,** *54* (5), 547-571.

31. Pittenger, B.; Erina, N.; Su, C., Quantitative mechanical property mapping at the nanoscale with PeakForce QNM. *Application Note Veeco Instruments Inc* **2010,** *1*, 1-11.
32. Derjaguin, B. V.; Muller, V. M.; Toporov, Y. P., Effect of contact deformations on the adhesion of particles. *Journal of Colloid and Interface Science* **1975,** *53* (2), 314-326.
33. Lapuerta, M.; Barba, J.; Sediako, A. D.; Kholghy, M. R.; Thomson, M. J., Morphological analysis of soot agglomerates from biodiesel surrogates in a coflow burner. *Journal of Aerosol Science* **2017,** *111*, 65-74.
34. Qian, Y.; Willeke, K.; Grinshpun, S. A.; Donnelly, J.; Coffey, C. C., Performance of N95 Respirators: Filtration Efficiency for Airborne Microbial and Inert Particles. *American Industrial Hygiene Association Journal* **1998,** *59* (2), 128-132.

Figures

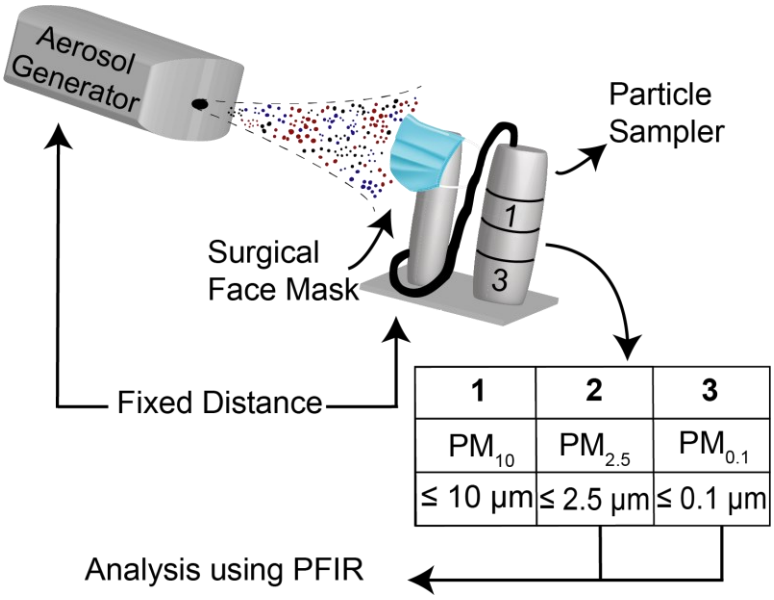

Figure 1. The scheme for production and collection of bioaerosols. A particle generator nebulizes a liquid solution of BSA at a fixed flow rate and distance toward a particle sampler with a surgical-grade facemask directly covering its inlet. The sampler distinguishes collected substances by the range of their diameters; with larger particles being trapped in the top-most chamber and the smallest in the bottom chamber. Bioaerosol particles impacted onto substrate inside the sampler are separated according to their aerodynamic diameters into three stages before the analysis using PFIR microscopy.

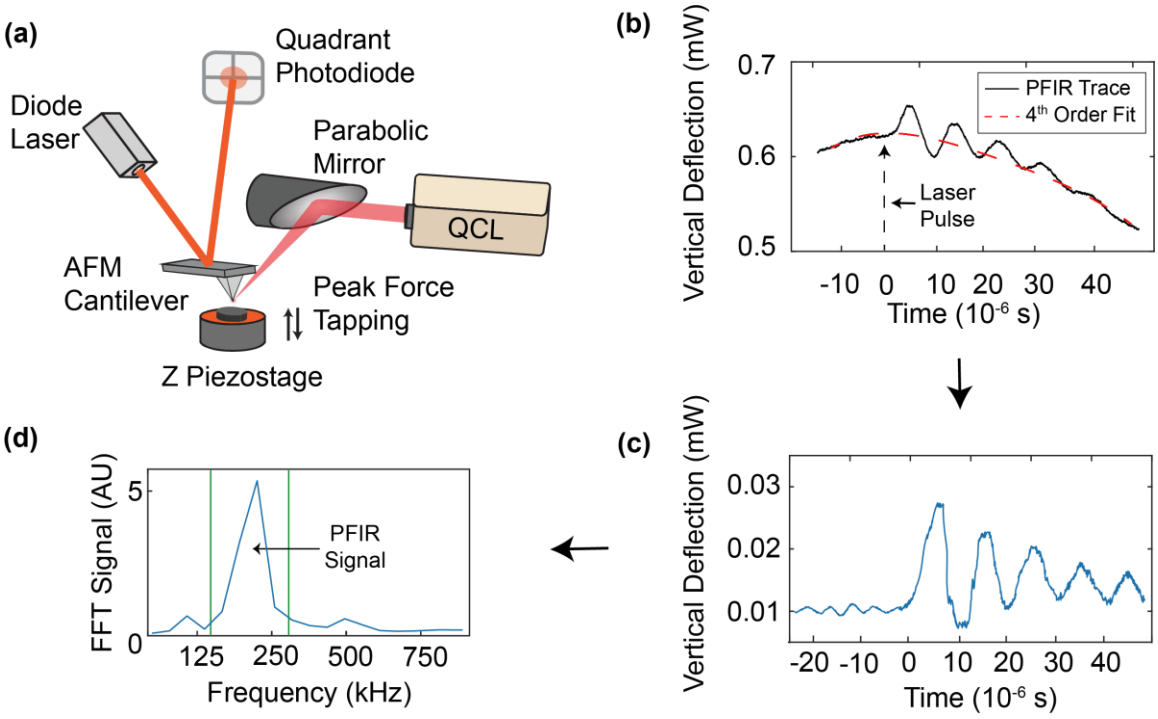

Figure 2. Schematic of PFIR apparatus and signal acquisition. (a) The hardware of the PFIR microscope consists of a stage scan AFM and frequency tunable light source. (b) The vertical deflection signal of the AFM cantilever when it is in dynamic contact with the sample surface (black line). Timing of the laser pulse Illumination is marked by a vertical dashed arrow. A fourth-order polynomial fit (red dashed curve) is used to subtract the baseline curvature due to tip indentation on the sample surface in the PFT cycle. (c) Extracted cantilever oscillations from the vertical deflection of the cantilever in (b) after baseline correction by polynomial fitting. (d) Fast Fourier-transform converts the cantilever oscillations into PFIR signal from panel (c).

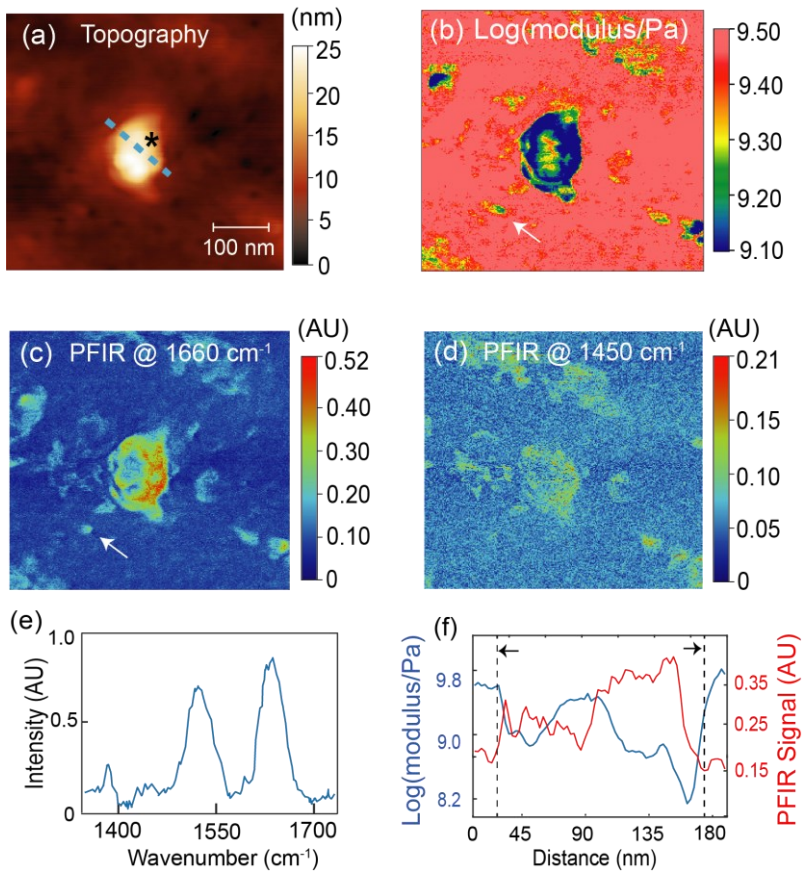

Figure 3. Display of chemical and mechanical properties of a lab-generated aerosol particle from BSA protein. (a) Topography. (b) Modulus. (c) and (d) are PFIR images taken at 1660 cm^{-1} (on resonance) and 1450 cm^{-1} (off-resonance), respectively. (e) A PFIR spectrum collected at the location marked by the star in (a). Characteristic infrared response of protein is observed. (f) Sectional plots of logarithmic modulus (blue) and PFIR signal at 1660 cm^{-1} (red) along the dashed line in (a). It reveals the heterogeneity of this aerosol particle, despite its small size. The white arrow in (c) points to an ultrafine aerosol of ~20 nm diameter.

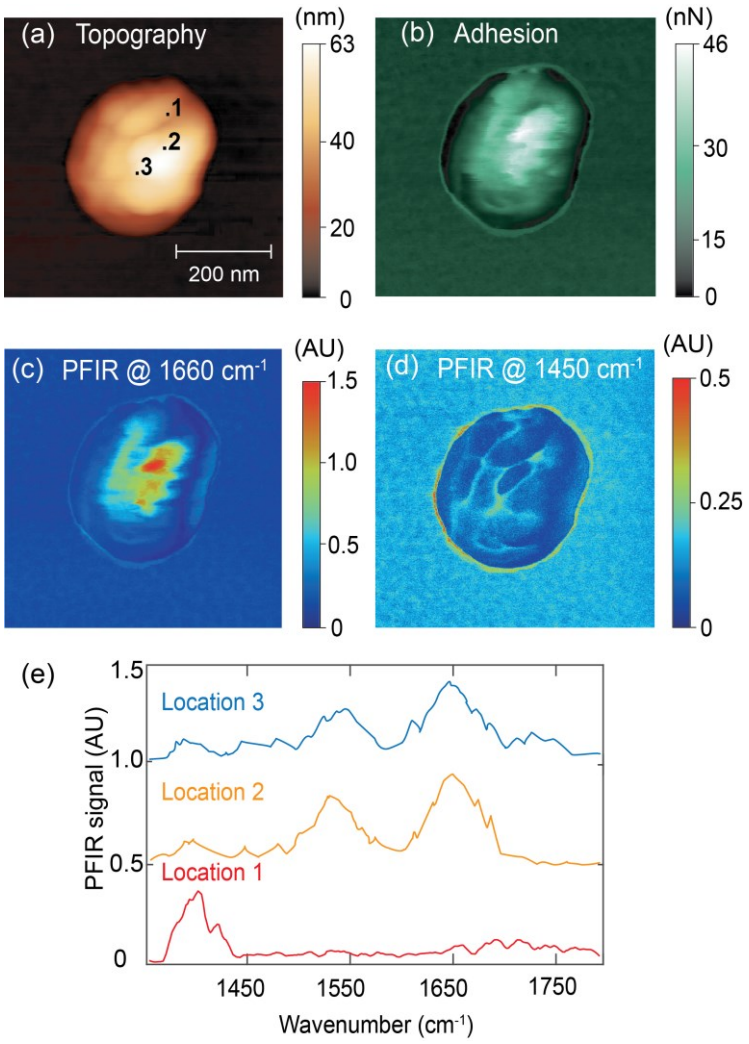

Figure 4. PFIR measurements of a field-collected indoor aerosol particle (a) Topography of the particle. (b) Adhesion map of the particle. (c) and (d) are PFIR images taken at the infrared frequency of 1660 cm^{-1} and 1450 cm^{-1}, respectively. (e) Point spectra were taken from three locations indicated by numbers 1-3 on panel (a). The spectra of locations 2 and 3 are vertically shifted by 0.5 and 1.0 AU in the plot for clarity.

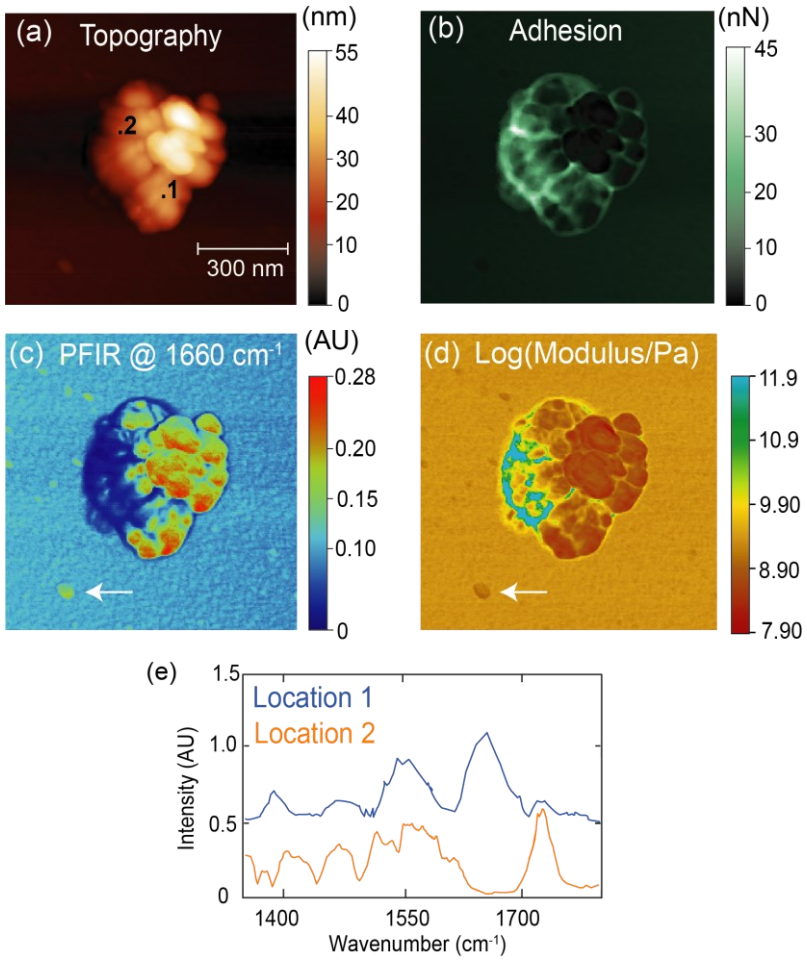

Figure 5. The PFIR measurement of a fine aerosol particle from the second stage of the aerosol collector. (a) Topography. (b) Adhesion, (c) Logarithmic of the modulus. (d) PFIR images at 1660 cm^{-1}. (e) Point spectra were taken from two locations indicated in panel (a). The spectrum of location 1 is vertically offset by 0.5 AU. The white arrows in (c) and (d) point to an ultrafine aerosol of ~50 nm in diameter.

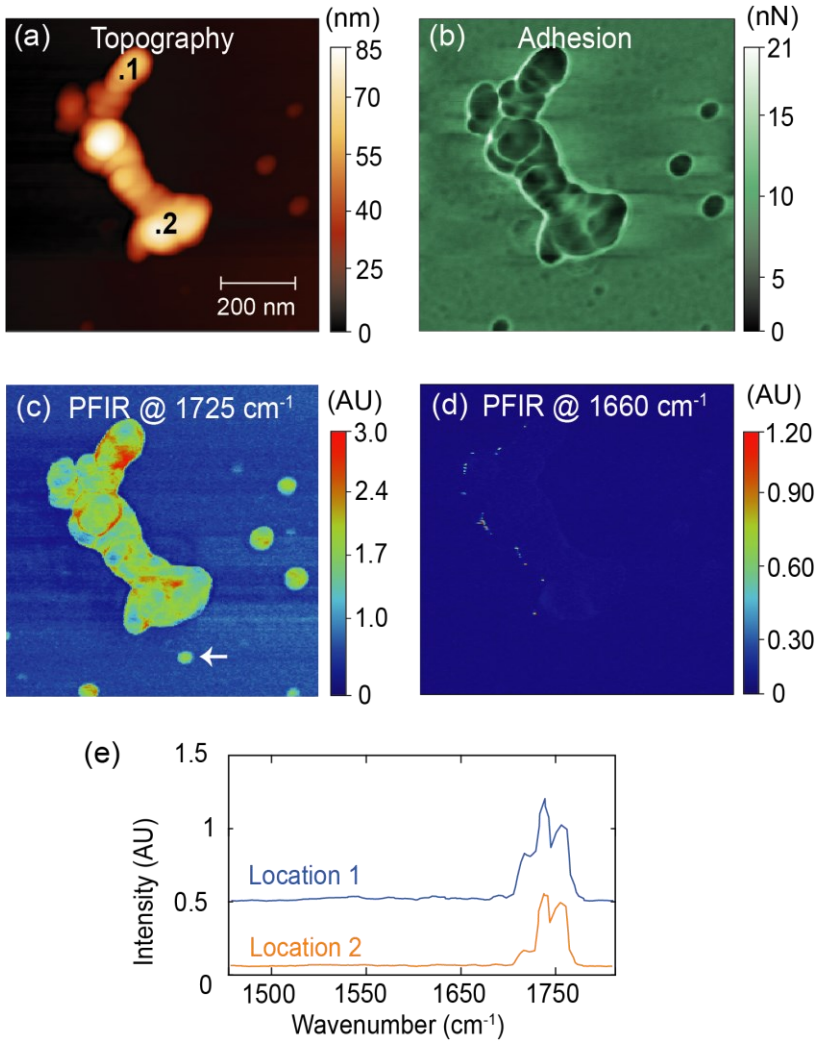

Figure 6. (a) Topography of the irregular shape aerosol particle, collected at the second stage of particle sample without filtration of a face mask. (b) The adhesion map of the aerosol particle. (c) The PFIR image at infrared frequency of 1725 cm^{-1}. The PFIR image reveals possible ultrafine aerosol detection capabilities as indicated by the arrow pointing towards a particle with roughly 50 nm lateral diameter and PFIR response of about 0.7 AU. (d) The PFIR image at the infrared frequency of 1660 cm^{-1}. (e) Two PFIR spectra were collected from locations marked in panel (a). The spectrum of location 1 is offset by 0.5 AU for clarity.

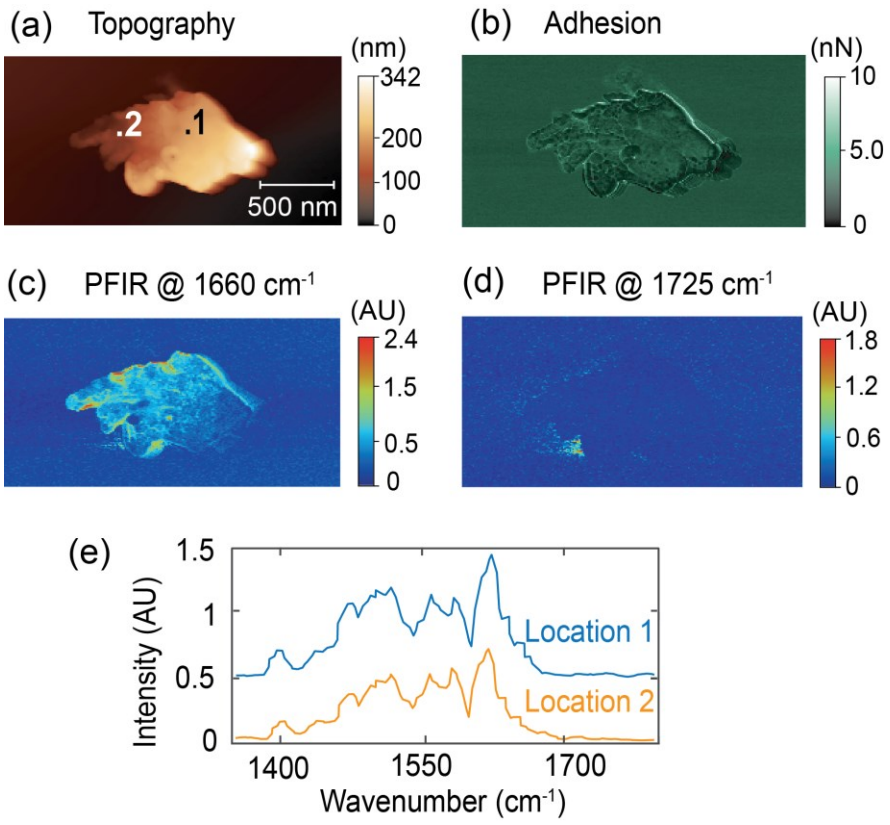

Figure 7. (a) Topography of an indoor aerosol particle of a flake shape. (b) Adhesion of the particle. (c-d) The PFIR images were taken at 1660 cm^{-1} and 1725 cm^{-1} infrared frequencies, respectively. (e) PFIR spectra from two locations on the aerosol particle. The spectrum of location 1 is vertically offset by 0.5 AU for clarity. The spectral signatures suggest biological origins.

TOC graphic

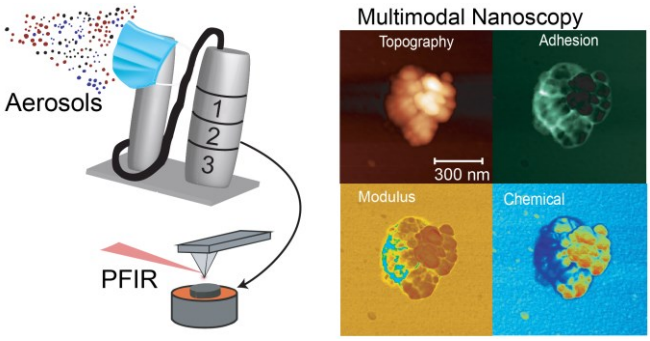
Aerosols
1
2
3
PFIR
Multimodal Nanoscopy
Topography
Adhesion
300 nm
Modulus
Chemical